






Comprehensive Measurements of the Volume-phase Holographic Gratings for the Dark Energy Spectroscopic Instrument

Yuzo Ishikawa^{1,2,3} , Martin M. Sirk^{1,2}, Jerry Edelstein^{1,2}, Patrick Jelinsky^{1,2}, David Brooks⁴ , and Gregory Tarle⁵ 
(DESI Collaboration)

¹ Space Sciences Laboratory, University of California, 7 Gauss Way, Berkeley, CA 94720, USA; yuzoishi@berkeley.edu

² Lawrence Berkeley National Laboratory, 1 Cyclotron Road, Berkeley, CA 94720, USA

³ Department of Physics and Astronomy, San Francisco State University, 1600 Holloway Avenue, San Francisco, CA 94132, USA

⁴ Department of Physics and Astronomy, University College London, Gower Street, London WC1E 6BT, UK

⁵ Department of Physics, University of Michigan, 450 Church Street, Ann Arbor, MI 48109, USA

Received 2018 July 16; revised 2018 October 18; accepted 2018 October 24; published 2018 December 7

Abstract

The Dark Energy Spectroscopic Instrument (DESI) is a Stage IV ground-based dark energy experiment that will be employed on the Mayall 4 m Telescope to study the expansion history of the universe. In the era of massively multiplexed fiber-fed spectrographs, DESI will push the boundaries of fiber spectroscopy with a design capable of taking 5000 simultaneous spectra over 360 to 980 nm. The instrument utilizes a suite of three-channel spectrographs, where volume-phase holographic (VPH) gratings provide dispersions. Thirty-six VPH gratings were produced and their performances were evaluated at the Lawrence Berkeley National Laboratory. We present the design and the evaluation tests for the production run of the VPH gratings, verifying the incidence angle, area-weighted efficiency, and wavefront errors (WFEs). We also present the specialized test set-up developed on-site to assess the grating performances. Measurements of the VPH gratings show high consistency in area-weighted efficiency to within an rms of 2% for the red and near-infrared and 6.2% for the blue gratings. Measured WFEs also showed high consistency per bandpass. Comprehensive evaluations show that the VPH gratings meet DESI performance requirements and have been approved for integration.

Key words: dark energy – instrumentation: spectrographs – techniques: spectroscopic

1. Introduction

One of the biggest developments in modern cosmology is the discovery of the accelerated expansion of the universe, first revealed through the measurements of Type Ia supernovae (Riess et al. 1998; Perlmutter et al. 1999). The nature of this accelerated expansion is not yet fully understood, but is believed to be driven by either a modification of general relativity or a new form of energy—*dark energy*, which contributes to nearly 70% of the universe’s energy density. The goal of the Dark Energy Spectroscopic Instrument (DESI) is to constrain the models of dark energy with a five-year galaxy and quasar redshift survey. Approximately 35 million redshifts will be obtained to measure the baryon acoustic oscillations and the growth of structure through redshift-space distortions (DESI Collaboration et al. 2016a). Results are expected to complement ongoing and future imaging surveys like the DESI Legacy Imaging Surveys, DES and LSST (LSST Science Collaboration et al. 2009; Abbott et al. 2018; Dey et al. 2018). DESI is currently under construction on the Mayall 4 m Telescope at the Kitt Peak National Observatory (DESI Collaboration et al. 2016a).

An overview of the telescope–instrument system and the optical layout of the spectrograph is illustrated in Figure 1. A suite of 5000 robotic fiber-positioners at the focal plane will take simultaneous spectra. The fibers are bundled into arrays of 500 that feed a suite of 10 three-channel spectrographs with resolution $R = \lambda/\Delta\lambda$ between 1500 and 4000, depending on wavelength (Edelstein et al. 2018; Poppett et al. 2016). Light from the fiber arrays is collimated by a spherical mirror, and then split into three spectral bandpasses using two dichroics. Each spectrograph channel houses a volume-phase

holographic (VPH) grating, which acts as the dispersion element optimized in its respective wavelength band. The wavelength bands are: blue (360–593 nm), red (566–772 nm), and near-infrared (NIR) (747–980 nm). The diffracted light is finally focused onto detectors by channel-specific cameras (Edelstein et al. 2018). Detailed descriptions of the DESI instrument designs and the science objectives are described in the DESI Final Design Reports and related literature (DESI Collaboration et al. 2016a, 2016b; Edelstein et al. 2018; Martini et al. 2018).

Given the scale and ambition of DESI, it is crucial that the dispersive elements not only provide sufficient throughput and preserve the imaging quality of the millions of spectra observed, but also have consistent performance to maximize the DESI spectrograph output. In this paper, we present the performance of the DESI VPH gratings measured at the Lawrence Berkeley National Laboratory (LBNL) test facilities. We first outline the design and science requirements of the gratings. Next we present the measurement methodologies, including the description of the custom measurement rig for the performance tests. We finally discuss the measurement results of the incidence angles, efficiency performances, and wavefront errors (WFEs).

2. VPH Gratings

VPH gratings have seen increased usage as dispersive elements in spectrographs due to their high-efficiency transmissive properties, and the ability to easily tune the blaze profile (Barden et al. 2000). The VPH gratings are constructed by sandwiching a thin gelatin film between two fused silica flat plates. The desired fringe frequency and orientation are

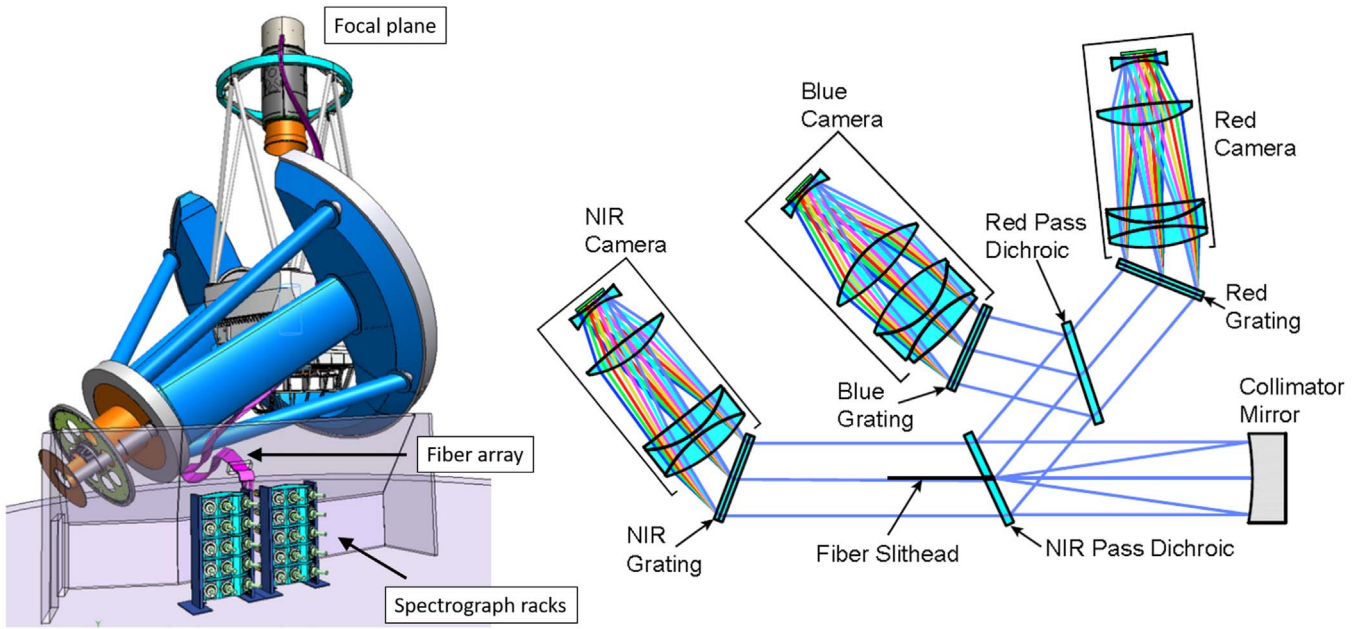


Figure 1. Schematic of DESI with the Mayall 4 m Telescope illustrating the fiber arrays from the focal plane feeding the spectrographs (left). Light from each fiber array follows the optical path through the red, blue, and near-infrared channels before reaching the channel-specific cameras illustrated (right). Diagrams from DESI Collaboration et al. (2016b).

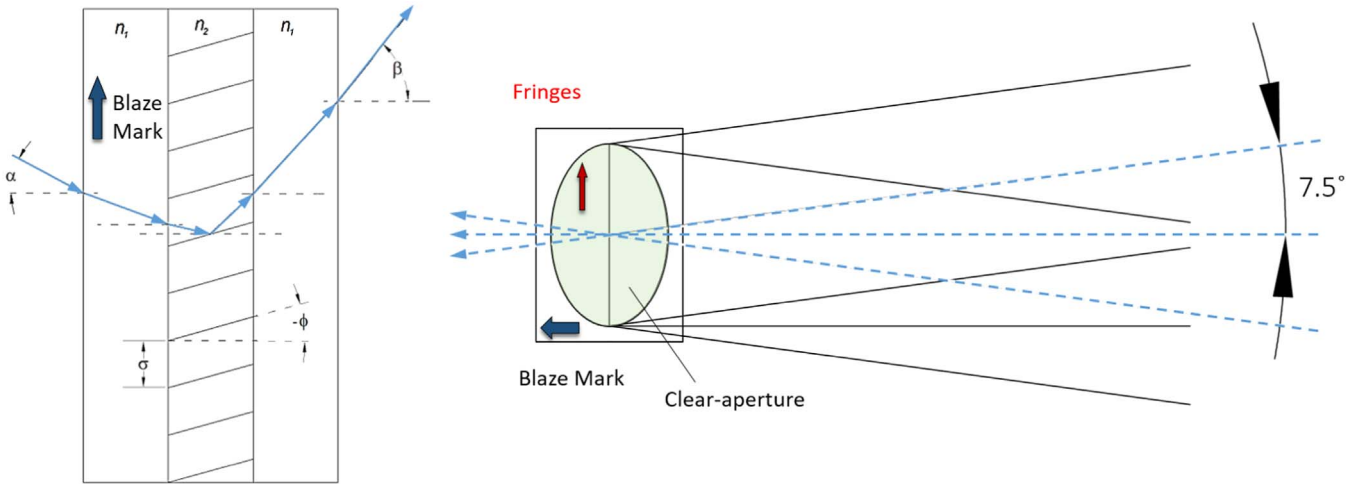


Figure 2. (Left) Cross-section of the VPH grating normal to the incident face and the fringe vector, where the fringes are slanted at angle $\phi \approx 3^\circ$ and the orientation of the blaze mark is indicated. Light is incident from the left at α . The grating package is antireflection coated on both faces. (Right) Range of off-plane angles incident on the VPH grating with the clear aperture marked. Light is incident from the right.

recorded via a holographic exposure system (Barden et al. 1998). Input light is diffracted due to the modulation pattern of the bulk refractive index, which changes the optical path (Arns et al. 1999; Blanche et al. 2006). The fringes of VPH gratings are typically tilted within the gelatin to remove the Littrow ghost, which may contaminate the primary diffraction (Burgh et al. 2007). The DESI gratings are tilted by roughly $\phi \approx 3^\circ$. Figure 2 schematically displays the structure and geometry of the gratings, where α is the incidence angle, β is the diffraction angle, and ϕ is the fringe tilt angle. An optimal incidence angle α_0 , satisfying the Bragg condition, is chosen such that the integrated diffraction efficiency of the gratings is maximized (Barden et al. 1998).

In addition to maintaining high throughput, the WFEs must be well accounted for, since sandwiching the VPH gelatin between glass plates can potentially distort and degrade the imaging quality through the grating (Barden et al. 2000, 2002). WFEs in VPH gratings can be caused by many factors, such as polishing errors of the substrates, bending of the substrate-gelatin stack due to residual stresses (e.g., cementing processes and thermal effects), or an imperfect holographic recording written directly into the gelatin (Barden et al. 2000, 2002; Blanche et al. 2006). Thus it is crucial to characterize both the diffraction efficiency and the WFEs at the order(s) of interest, especially when high consistency is required for large-scale surveys like DESI. Further discussion of the VPH grating physics is given by Barden et al. (1998).

Table 1
DESI VPH Grating Specifications and Requirements for Unpolarized Incidence; Wavefront Specifications at 632 nm

Specification	Blue	Red	NIR
λ range	360–593 nm	566–772 nm	747–980 nm
Fringe frequency	1103.5 \pm 2 1/mm	1157.4 \pm 2 1/mm	992.5 \pm 2 1/mm
Clear aperture	136.4 mm	140.6 mm	146.0 mm
Pupil diameter	131.0 mm	136.0 mm	137.5 mm
Central incidence α_0^a	$-10^\circ.46$	$-18^\circ.12$	$-20^\circ.76$
+1 order VPH grating efficiency ^b	>65%	>80%	>80%
Exterior AR coatings reflection per face	<0.6%	<0.5%	<0.5%
+1 order VPH grating efficiency (adjusted) ^c	>64.2%	>79.2%	>79.2%
Diffacted wavefront, Irregularity P-V	1 wave	1 wave	1 wave
Diffacted wavefront, Power P-V	1.5 waves	1.5 waves	1.5 waves

Notes.

^a Incidence angles are to be within an allowed installation range of $\pm 1^\circ 0$ from the specified α_0 (Edelstein et al. 2018).

^b Including glue and gelatin losses, not including AR coating and glass transmission losses.

^c Adjusted for glue, gelatin, AR coating, and glass transmission losses. We compare measurements to these values.

2.1. Requirements and Specifications

The DESI VPH gratings have physical dimensions of $180 \times 160 \text{ mm}^2 \times 16 \text{ mm}$ (thickness) with varying clear aperture areas. The incident field of view (FOV) of the grating is $\pm 7^\circ.5$ from the grating central axis, illustrated in Figure 2, and is illuminated by a collimated beam of various pupil sizes. All DESI VPH gratings are optimized such that the +1 diffracted order efficiency is maximized. There were no specifications on off-axis FOV efficiency. The performance requirements and specifications for the DESI VPH gratings are detailed in Table 1. These are driven by both science requirements and optical design limitations. Efficiency requirements listed are averaged over polarization and over the clear aperture. Since the actual measurements of the diffraction efficiency will include transmission losses from the VPH gelatin, glue, antireflection (AR) coating, and the substrate glasses, the “adjusted” efficiencies are used to compare results. A total of 36 full-size gratings (12 per channel) were produced by Kaiser Optical Systems Inc. (KOSI). A preliminary set of measurements was conducted by KOSI on a few points across the clear aperture (Figure 4), albeit in a less comprehensive manner compared to our measurements presented here. Based on our measurements, the top performing gratings in each channel with the best efficiencies are chosen for DESI integration.

2.2. Preliminary Evaluation of Test Gratings

Prior to the full production of the DESI VPH gratings, preliminary performance studies were conducted on full-size test VPH gratings for each bandpass, also produced by KOSI. Measurements were made in all three bandpasses to verify that the gratings met desired design specifications and also to prototype a set of reliable and efficient test procedures discussed in this paper. Efficiency performance at the specified incidence angle and the peak-to-valley (P-V) WFE for power and irregularity met the requirements (DESI Collaboration et al. 2016b). Performance results of the test gratings were used to constrain the properties of the final DESI VPH gratings discussed in this paper.

3. Measurement Rig

We built an automated optical test bench to measure the +1 order diffraction efficiency of the gratings. The design was motivated by the desire to conduct a comprehensive yet efficient performance characterization across the entire clear aperture, while minimizing the handling of the VPH gratings. This test rig allows us to determine the optimal incidence angles, to perform a full-grating scan, and to illuminate off-axis angles. The rough design is inspired by the tunable spectrograph concept outlined in Barden et al. (1998): a source output is collimated into a narrow pencil beam to illuminate the grating, and the diffracted light is captured by a detector. A schematic and photograph of the measurement rig are shown in Figure 4. All measurements using the rig were conducted inside a dark tent.

A set of six Mightex LEDs at discrete wavelengths ($\lambda = 365, 385, 400, 470, 505, \text{ and } 560 \text{ nm}$) are used to illuminate the blue gratings, and a Newport 1/8 m monochromator is used for the red and NIR gratings. The Mightex LEDs are used since they provide much higher flux in the UV–blue range in contrast to the monochromator. Narrow-pass filters are installed in the LEDs to produce beams with typical FWHM of 10 nm. The output from the LEDs is fed through a 200 μm diameter multi-mode fiber to a 10 mm focal length collimator, which produces a 5 mm diameter beam at the grating. For the red and NIR measurements, the monochromator is illuminated with a bright tungsten lamp, and a set of broadband filters at the input block-out second-order contamination. Because of the low output flux, the monochromator light is fed through a larger 400 μm diameter, 1 m long multi-mode fiber, which produces a 10 mm diameter beam at the grating. We did not actively control or measure the polarization of the light incident on the grating, as polarization effects were not an issue for the DESI project. We estimate the degree of polarization incident on the gratings, and its consequences in Section 6.1.

The VPH grating is mounted on dual co-axial rotation stages that independently rotate the grating and the photodiode detector. Rotating the grating sets the incidence angle α of the collimated beam incident on the grating. The collimator is mounted on a tip-tilt stage that aligns the beam to grating normal within $\pm 0^\circ.07$. An integrating sphere and photodiode

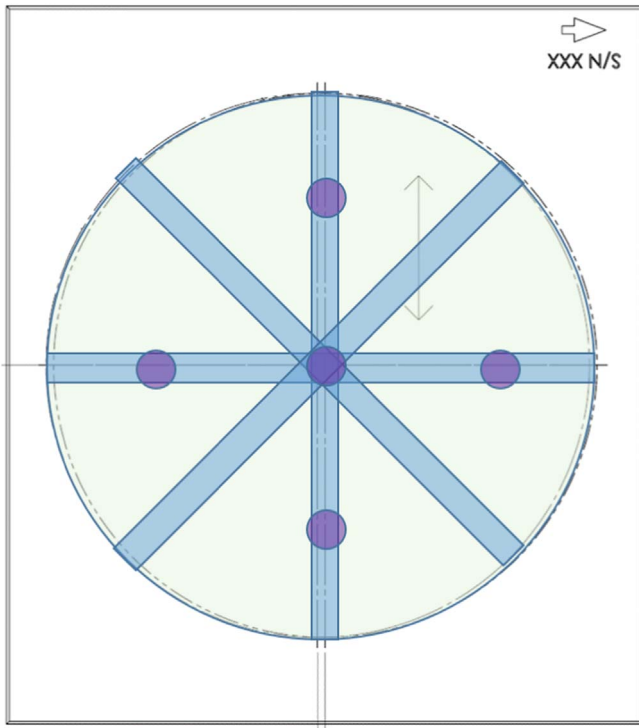


Figure 3. Sweep regions across the VPH grating as seen from the incidence face. Green marks the clear aperture and the blue strips mark the approximate full-grating sweep regions. The purple circles mark the five regions measured by KOSI.

detector assembly, mounted on the extended arm from the rotary stages, captures and centers the diffracted beam at the corresponding output β -angle to within $0^{\circ}.01$. The beam intensity is measured using a Newport 1936-R power meter. Employing a tubular black paper baffle around the integrating sphere input port greatly improves the signal-to-noise ratio to make quick initial verification in the presence of background light and allows the control computer monitor to be used inside the dark tent.

Both the photodiode assembly and the input beam fiber collimator are mounted on vertical translation stages that change the height of the incident beam. Similarly, the grating mount is secured on a linear translation stage that translates the grating laterally to the beam without changing either α or β . By synchronizing the horizontal and vertical motions of the grating, beam collimator, and detector, we are able to scan different regions of the grating active area at constant α and β , as shown in Figure 3. In addition, the beam collimator and detector are mounted on swivel stages that pitch the beam at $\pm 7^{\circ}.5$ to simulate the off-axis FOV inputs illustrated in Figure 2. All measurement rig motions and data acquisition processes are fully automated with custom Python software. This allows us to quickly obtain full-grating efficiency performance evaluations.

4. Measurement Procedure

Each grating was inspected to identify visible defects, and then it was placed in the measurement rig with the blaze marker in the correct orientation before rigorous performance tests. Measurement goals were as follows.

1. Optimal incidence angle at grating center. As discussed in Section 2, the integrated absolute diffraction efficiency

$H_{\alpha}(\lambda)$ across a given wavelength band is maximized at the optimal incidence angle α_0 . To accomplish this, a collection of absolute efficiencies are obtained for 5–6 different λ across the bandpass at various α to calculate $H_{\alpha}(\lambda)$ at the grating center. The absolute diffraction efficiency is the ratio of the +1 order diffraction measurement to the through-beam measurement. The fiber collimator and the photodiode detector are driven upwards so that the beam travels over the grating for through-beam measurements. Then the two components are driven back down, and the grating and detector are set at appropriate α and β angles for the +1 order grating diffraction. Different α measurements are conducted by rotating the grating at $0^{\circ}.5$ steps at fixed λ . This process is repeated for each λ .

2. Full-grating area-weighted efficiency at α_0 . Once α_0 is determined at the grating center, relative efficiencies with respect to grating center are measured via horizontal, vertical, and cross-diagonal scans at α_0 . Scans through the grating center are taken at 0.25 inch intervals, such that the beam diameter partially overlaps the adjacent measurements. Approximate sweep regions are shown in Figure 3. Although it is possible to survey the entire grating area, initial analysis showed that our scans were sufficient for performance evaluations. These measurements allow us to quickly calculate the average area-weighted efficiency of the grating for the entire active area.

3. Wavefront errors. The VPH gratings are installed in a different setup employing a Zygo interferometer to measure the power and irregularity components of the transmitted WFEs. A Zygo interferometer is put in place of the input light in Figure 4, and the photodiode is replaced by a large flat return mirror to create a double-pass measurement of a VPH grating at the $m = +1$ order. A 4 inch diameter, 632.8 nm HeNe beam from the Zygo illuminates the VPH clear aperture. The gratings are installed on a mount with large frames, which severely limit the range of allowed incidence angles and the measurable clear aperture. As a result, the blue, red, and NIR gratings are illuminated at roughly -29° , -40° , and -50° respectively, which wildly differ from the design α_0 listed in Table 1 ($-10^{\circ}.46$, $-18^{\circ}.12$, and $-20^{\circ}.76$ respectively). Unfortunately, the incidence angles were arbitrarily chosen to prevent the incident and transmitted beams from getting clipped by the mount frames. Because of this complication, we did not take additional steps to fully cover the grating clear aperture. Also the Zygo wavelength is out-of-band for the blue and NIR gratings. However, measurements showed that the gratings have sufficient 632.8 nm efficiency for high signal-to-noise measurements. The WFE maps of each VPH grating are recorded using the Zygo software. The return mirror flatness is known to be $< \lambda/20$ as per LBNL optics shop specifications. Since the allowed DESI WFE budget was substantially larger than $\lambda/20$, reference measurements of the return mirror were not taken.

5. Grating Performance

5.1. Optimal Incidence Angle at Grating Center

Absolute efficiency measurements performed at a series of different wavelengths and α produce a set of efficiency versus wavelength ($\eta_{\alpha}(\lambda)$) relations, often called “rocking curves.” Figure 5 shows example sets of rocking curves for typical blue, red, and NIR gratings measured at the grating center. Each dotted-line curve represents a set of measurements made at

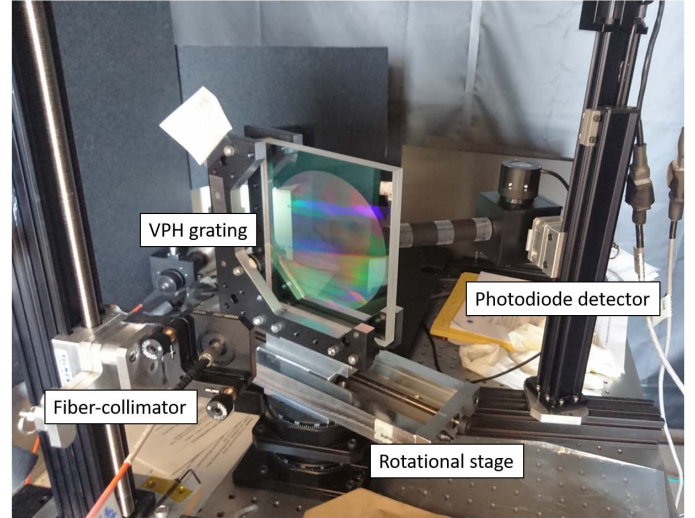
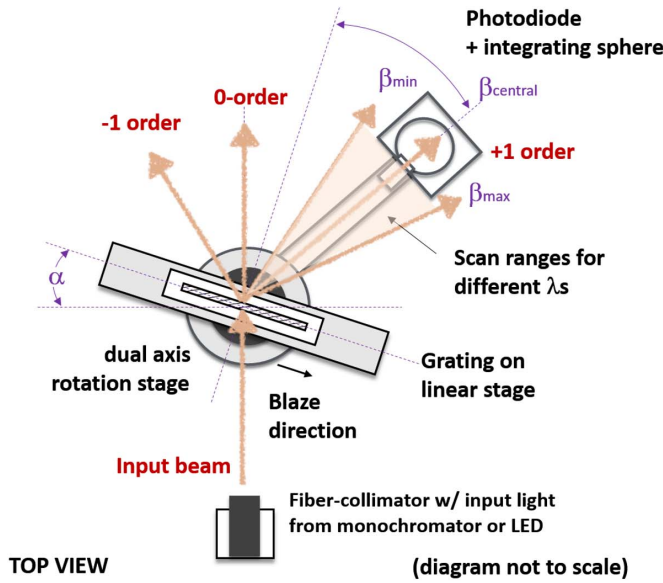


Figure 4. Schematic (left) and photograph (right), as seen from the incident face, of the VPH grating measurement rig.

discrete α -angles separated by 0.5° . A full suite of rocking curves is available from the first author.

To determine the optimal α_0 , first a spline interpolation is performed on each set of discrete $\eta_\alpha(\lambda_i)$ data points to produce a continuous $\eta_\alpha(\lambda)$ curve. Then the integrated efficiency of each curve is calculated by $H_\alpha(\lambda) = \int \eta_\alpha(\lambda) d\lambda$, which produces a set of $H_\alpha(\lambda)$ and α pairs. We take the maximum of the parabolic interpolation of the H_α versus α relation, which corresponds to the optimal α_0 for a given grating, shown in Figure 5. This is repeated for each grating.

The averages of the measured α_0 s were $\alpha_0 = -11.7^\circ$, -18.42° , and -21.47° for the blue, red, and NIR gratings respectively. The measured incidence angles for the red and NIR gratings were within the allowed installation window of $\Delta\alpha_0 = \pm 1.0^\circ$; however, all of the top 10 blue gratings were not. Because of this, the reported α_0 for the blue gratings were set to the maximum allowed angle of -11.5° . Subsequent full-grating sweeps for the blue were performed at $\alpha_0 = -11.5^\circ$, while the red and NIR gratings tests were performed at the measured optimal α_0 angles.

Finally, the rocking curves for the interpolated optimal α_0 are calculated by taking the weighted average of the two adjacent rocking curves with discrete data, which are shown as solid red curves in Figure 5. For example, the $\eta_{\alpha_0}(\lambda)$ curve for the blue is the weighted average of the -11.5° and -12° curves. The optimal $\eta_{\alpha_0}(\lambda)$ curves are used to calculate the area-weighted efficiency, and also serve as quick initial examination of the grating performance to first order, making the grating center performance a good indicator for predicting the overall efficiency performance. In addition, highly sampled 40 λ measurements are obtained for a few red and NIR gratings to better model the efficiency profile for subsequent analysis. The average α_0 of the 10 best gratings per channel is summarized in Table 2, and all measured α_0 are listed in Tables 3–5.

5.2. Full-grating Area-weighted Efficiency

A series of full-grating scans at the optimal α_0 were conducted to calculate the area-weighted efficiency and the

wavelength-averaged efficiency, which characterize the overall performance. Data were initially taken at 5–6 λ ; however, initial analysis showed that 3 λ measurements that bound the center and edges of the wavelength bands were sufficient for subsequent full-grating sweeps. This expedited the process of measuring 36 gratings. Figure 6 shows example scans of the full-grating sweeps, plotting measured efficiencies relative to the grating center. Absolute efficiency values are obtained by scaling the relative efficiency values by the appropriate $\eta_{\alpha_0}(\lambda)$ relations calculated in Section 5.1.

Using the absolute efficiency values across the clear aperture, we calculate the area-weighted efficiency for each grating. First, we average the set of efficiencies corresponding to the same radius from the grating center and obtain an average absolute efficiency versus radius relation as shown in Figure 7. From the trends in Figures 6 and 7, we note that the radial efficiency is mostly constant near the grating center; however, a wavelength-dependent spread is observed toward the edge of the grating clear aperture. Then we scale the average local efficiencies by the annular area bounded by each measured radii to obtain fractional area-weighted efficiencies. The sum of the fractional efficiencies is the area-weighted efficiency, $\eta'(\lambda)$.

Since some wavelength measurements were not sampled for expediency, $\eta'(\lambda)$ for the missing wavelengths was calculated by fitting the highly sampled $\eta'(\lambda)$ curves to the low-sampled $\eta'(\lambda)$ data points for each grating. First, the highly sampled curves are interpolated to create model rocking curves (the 5–6 λ points for the blue, and the 40 λ measurements for the red and NIR). Then the models are scaled to the 3 λ data points, using scaling values determined from least-squares fitting, to create continuous $\eta'(\lambda)$ relations. The measured and interpolated $\eta'(\lambda)$ for all gratings are shown in Figure 8 overplotted with the average $\eta'(\lambda)$ relation of the grating sets in the respective bandpass. Figure 9 plots the average $\eta'(\lambda)$ curves for the three channels and compares against vendor predictions (J. Arns 2018, private communication). Thus these $\eta'(\lambda)$ serve as the effective rocking curves for each grating.

Finally, the wavelength-averaged, area-weighted efficiency $\bar{\eta}_\lambda$ is calculated to characterize the overall grating performance

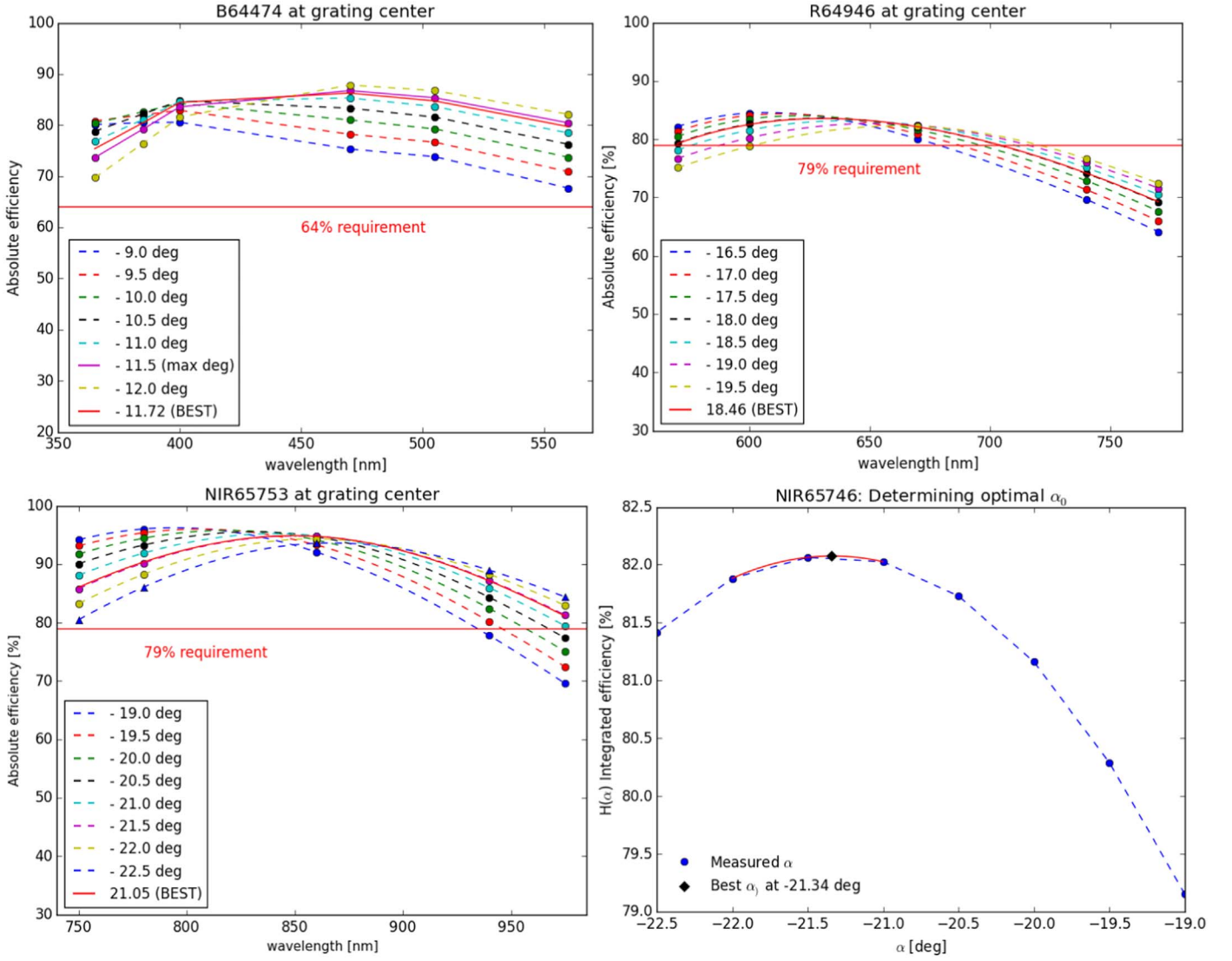


Figure 5. Example rocking curves measured at the grating center: blue (top left), red (top right), and NIR (bottom left). The solid lines represent the interpolated $\eta_{\alpha_0}(\lambda)$ for α_0 . The parabolic interpolation determines the maximum of $H_{\alpha}(\lambda)-\alpha$, which yields α_0 (bottom right). Uniformity in the spacing of individual points for different α indicates a small relative error of $<1\%$.

Table 2
Averaged Performances of the Top 10 Gratings in Each Bandpass, Listing the Measured α_0 , the Wavelength-averaged Area-weighted Efficiency $\bar{\eta}_{\lambda}$, and the Corresponding rms Variation $\sigma_{\eta(\lambda)}$ and Uncertainty $\bar{\sigma}_{\eta(\lambda)}$

Grating	λ min (nm)	λ central (nm)	λ max (nm)	α nominal (deg)	α_0 measured (deg)	$\bar{\eta}_{\lambda}$ (%)	$\sigma_{\eta(\lambda)}$ (%)	$\bar{\sigma}_{\eta(\lambda)}$ (%)
Blue	360	470	593	$-10^{\circ}46$	$-11^{\circ}7$	75.1	± 6.1	± 1.9
Red	566	669	772	$-18^{\circ}12$	$-18^{\circ}43$	76.8	± 1.98	± 0.63
NIR	747	860	980	$-20^{\circ}76$	$-21^{\circ}47$	85.2	± 1.41	± 0.45

and to rank the gratings for final selection. The $\bar{\eta}_{\lambda}$ is obtained by averaging $\eta'(\lambda)$ for each λ measured or interpolated. The detailed average performance results for all gratings are presented in Tables 3–5. The averaged $\bar{\eta}_{\lambda}$ for the top 10 grating sets for each band are also summarized in Table 2 with the corresponding rms variation and uncertainty.

The measured $\bar{\eta}_{\lambda}$ is the combined efficiency of the grating diffraction, and the AR coating, glass, and gelatin transmission efficiencies, so we compare $\bar{\eta}_{\lambda}$ to the adjusted DESI efficiency requirements in Table 1. The measured $\bar{\eta}_{\lambda}$ summarized in

Table 2 show that the blue and NIR gratings sufficiently satisfy the adjusted efficiency requirements. However, the averaged red efficiency of 76.8% is slightly below the DESI requirement by 2.4%. This drop in efficiency is caused by the sharp drop in performance in the $740 \text{ nm} < \lambda < 770 \text{ nm}$ band where the $\bar{\eta}_{\lambda}$ range between 65% and 75%, as seen in Figures 5 and 8. In fact, the the red gratings' deficiency in the 740–770 nm band may affect the signal-to-noise of the measured galaxy spectra in distinguishing emission-line features for redshift measurements, which is important for the DESI surveys

Table 3
Performance of All 12 Blue Gratings Measured

Grating SN	α_0 (deg)	365 nm (%)	385 nm (%)	400 nm (%)	470 nm (%)	505 nm (%)	560 nm (%)	$\bar{\eta}_\lambda$ (%)
64478	-11°8	78.9	82.2	84.2	88.3	87.1	80.7	83.6
64476	-11°7	77.2	82.4	86.7	87.3	76.7	76.7	82.4
64477	-12°0	78.6	81.0	82.5	85.3	84.2	79.1	81.8
64474	-11°7	73.1	78.5	82.8	86.3	84.5	78.9	80.7
64470	-11°7	73.4	76.9	79.9	80.4	76.4	68.1	75.9
64475	-12°1	65.4	68.4	70.3	74.8	74.5	70.6	70.7
64473	-11°8	68.7	71.1	72.5	73.6	71.0	62.5	69.9
64472	-11°8	69.5	71.8	73.0	73.1	69.7	59.6	69.4
64469	-11°6	70.1	71.9	72.8	72.2	69.0	60.0	69.3
64467	-11°7	62.7	65.9	67.9	71.9	70.7	64.4	67.3
64468	-10°3	63.9	66.7	68.3	70.5	68.2	60.1	66.3
64471	-12°0	65.4	66.9	67.6	67.4	64.9	57.9	65.0
Average	-11°7	70.6	73.9	75.6	77.6	75.2	68.2	73.5
rms	$\pm 0^\circ 4$	± 5.5	± 6.0	± 6.6	± 7.1	± 7.4	± 8.3	± 6.8

Table 4
Performance of all 12 Red Gratings Measured

Grating SN	α_0 (deg)	570 nm (%)	600 nm (%)	670 nm (%)	740 nm (%)	770 nm (%)	$\bar{\eta}_\lambda$ (%)
64942	-18°48	85.16	86.90	85.61	76.82	70.76	81.05
64939	-18°56	79.27	82.77	84.49	77.88	73.46	79.57
64945	-18°50	77.68	82.00	83.09	75.47	70.47	77.74
64946	-18°46	79.13	81.56	81.73	74.20	68.62	77.05
64940	-18°22	77.49	81.22	81.38	73.30	68.28	76.33
64936	-18°38	79.67	81.36	80.00	71.22	65.19	75.49
64935	-18°66	77.20	80.11	80.03	72.33	67.54	75.44
64938	-18°36	79.54	81.10	79.69	71.21	65.41	75.39
64944	-18°37	79.27	81.08	79.93	71.24	65.21	75.35
64941	-18°29	77.69	79.70	79.11	71.14	65.46	74.62
64943	-18°65	75.98	78.20	78.12	70.66	65.20	73.63
64937	-18°33	78.18	79.09	76.85	68.49	63.04	73.13
Average	-18°44	78.93	81.17	80.83	72.51	67.37	76.16
rms	$\pm 0^\circ 13$	± 2.19	± 2.09	± 2.45	± 2.63	± 2.9	± 2.45

Table 5
Performance of all 12 NIR Gratings Measured

Grating SN	α_0 (deg)	750 nm (%)	780 nm (%)	860 nm (%)	940 nm (%)	975 nm (%)	$\bar{\eta}_\lambda$ (%)
65749	-21°27	86.01	89.42	93.37	86.26	80.45	87.10
65750	-21°56	83.73	88.58	93.70	87.45	81.14	86.92
65748	-21°41	89.42	92.51	93.36	83.48	75.78	86.91
65753	-21°05	86.36	90.33	92.37	87.10	77.70	86.16
65751	-21°66	86.17	89.94	91.67	84.43	75.29	85.10
65754	-21°97	77.03	84.43	93.77	87.97	80.67	84.77
65744	-21°67	85.69	90.39	90.52	82.66	73.18	84.49
65745	-21°06	71.35	79.81	92.40	90.50	85.12	84.84
65755	-21°82	82.83	87.56	91.30	82.12	74.05	83.57
65752	-21°16	84.21	87.53	89.30	80.76	73.78	83.12
65747	-21°56	82.68	85.27	85.86	77.26	70.61	80.34
65746	-21°34	83.40	84.79	82.84	72.64	65.58	77.85
Average	-21°46	83.25	87.46	90.89	83.17	76.1	84.17
rms	$\pm 0^\circ 29$	± 4.58	± 3.37	± 3.25	± 4.59	± 5.07	± 4.17

(DESI Collaboration et al. 2016a). Unfortunately, we do not know the source of this throughput loss. Despite this, consistency in the measured efficiency and the rocking curves

over all gratings in each bandpass was given more weight in evaluating the grating performance. Although the measured 76.8% red efficiency is not ideal, it was deemed to be

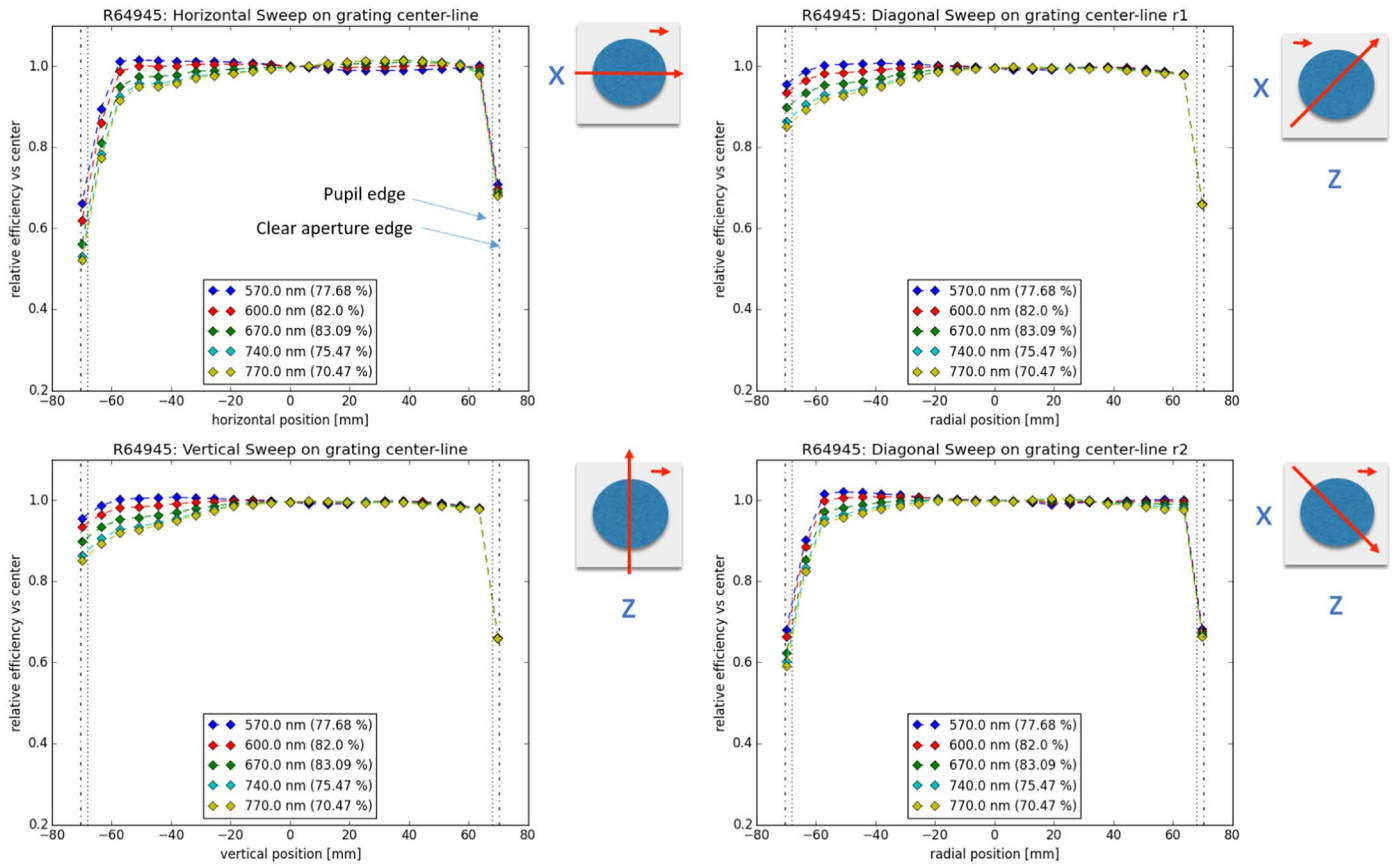


Figure 6. Example plots showing the relative efficiency values with respect to the grating center through the horizontal (top left), vertical (bottom left), and cross-diagonal (right top/bottom) sweeps for typical red gratings.

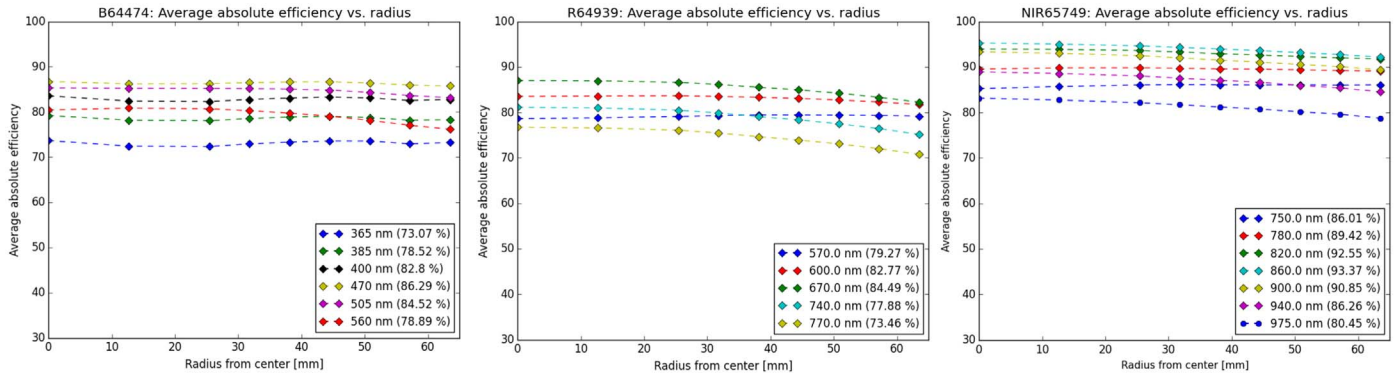


Figure 7. Example set of the average local absolute efficiency vs. radius from the grating center for typical blue (left), red (center), and NIR (right) gratings.

satisfactory for the DESI spectrograph integration. We note that the measured efficiency satisfies the DESI requirements at the central wavelengths (470, 670, and 860 nm) for all gratings.

5.3. WFE

The WFE maps were recorded and also analyzed using the Zygo Mx-Pro analysis software. A Zernike fringe polynomial fit was performed on the recorded WFE maps to extract the measured WFEs. By default, the Zygo Mx-Pro produces robust P-V (PVR) WFEs based on a 36-term Zernike fit defined by Evans (2008, 2009). These PVR values were corrected to

produce a standard P-V WFE and corresponding rms, which we use to compare with the DESI specifications (Table 1). Figure 10 shows an example set of the power and irregularity wavefront maps for each grating type.

However, since the test configuration, as described in Section 4, measured the WFE at different incident angles than what they were designed for, the measured P-V WFEs were corrected accordingly. In fact, the geometry of the test setup (e.g., the incidence angle and double-pass) acts to scale the overall measured WFEs (Bass 1994). The double-pass resulting from reflections off the return mirror doubles the measured WFEs, and the change in incidence angle compounds a $\cos \alpha$

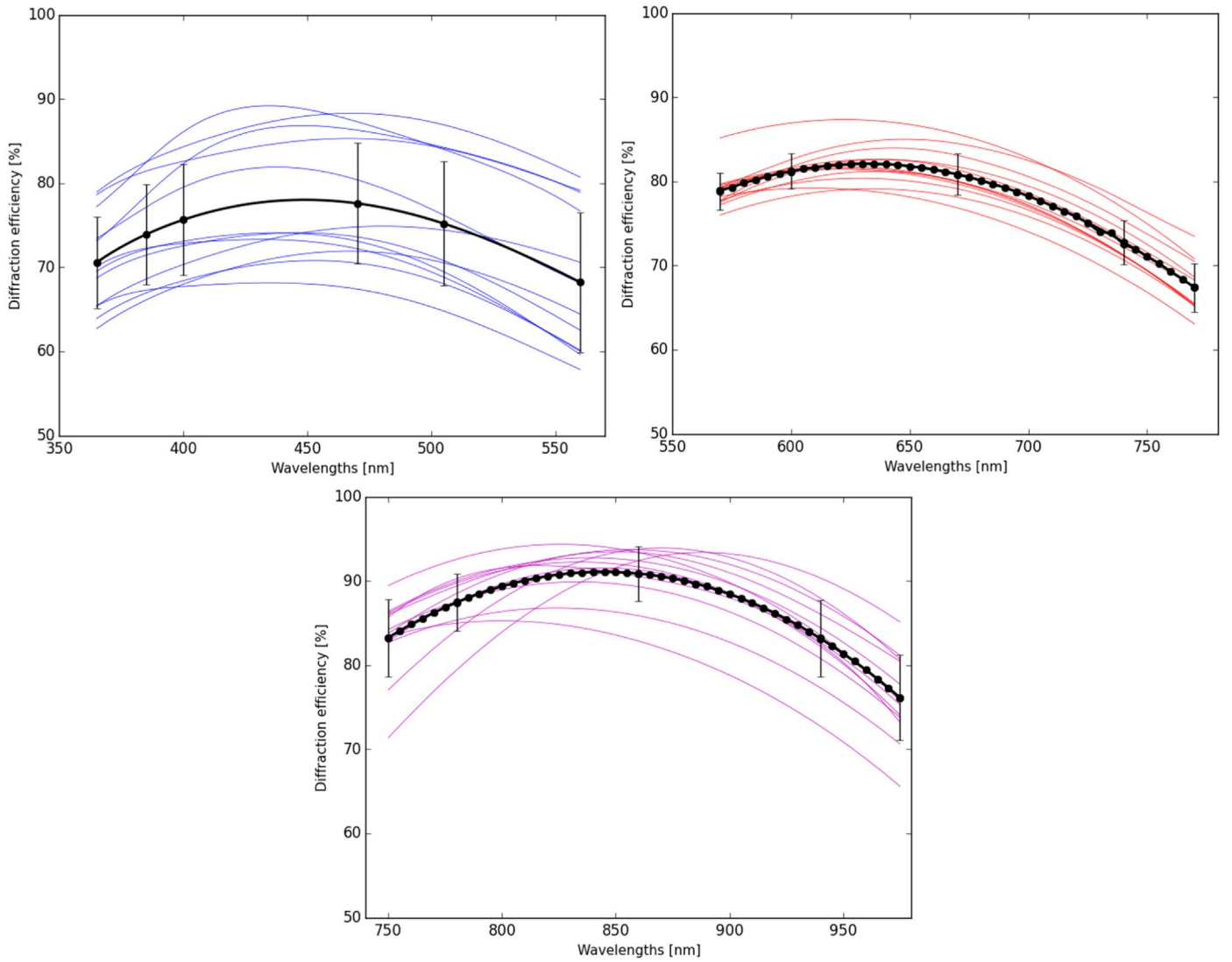


Figure 8. Area-weighted efficiency curves of the blue (top left), red (top -right), and NIR (bottom) gratings. The solid black curves indicate the average $\eta(\lambda)$, where the error bars represent the rms variations in measured efficiency. The highly sampled 40 λ models for the red and NIR gratings are scaled to the data points to produce the interpolated $\eta(\lambda)$ relations.

factor. The correction into single-pass WFEs measured at the desired incidence angle α_0 involves scaling the measured P-V WFEs by the scale factor

$$W = \frac{1 \cos \alpha_0}{2 \cos \alpha'} \quad (1)$$

where α' denotes the incidence angles chosen for the Zygo measurement (Bass 1994; Zecchino 2014). The W -factor corrections show that the biggest contribution to the additional WFEs comes from the double-pass scaling. On average, the measured P-V WFEs for the blue, red, and NIR gratings respectively, require roughly 56%, 62%, and 73% scaling correction. The corrected P-V power and irregularity WFEs for each VPH grating are listed in Tables 6–8. We see that the P-V WFEs for all 36 gratings are well within the DESI specifications of one wave for irregularity and 1.5 waves for power. No obvious correlation between the measured P-V WFEs and the measured average grating efficiency for each grating is observed.

6. Discussion

6.1. α -angle Accuracy and Tuning

As demonstrated by the incidence angle measurements in Figure 5, our ability to accurately characterize the efficiency profile of the VPH gratings is dependent on the accuracy of the measured α_0 . Errors in α_0 would mischaracterize the diffraction efficiency by biasing the rocking curve toward one side of the wavelength band (Barden et al. 2000). Measurement errors in α_0 are a consequence of uncertainties due to the optical alignment of the measurement rig (grating-to-beam alignment, accuracy of the rotational stages of the grating and photodiode detector) and the stability of the source (intensity and wavelength calibration).

The average uncertainty efficiency due to detector sensitivity is $\sigma_\eta = \pm 2\%$ for a measurement run, which is highlighted by the uniformity in efficiency measurements per wavelength for the different α angles plotted in Figure 5. An extensive wavelength calibration of the LEDs and the monochromator was performed against known emission lines from a neon

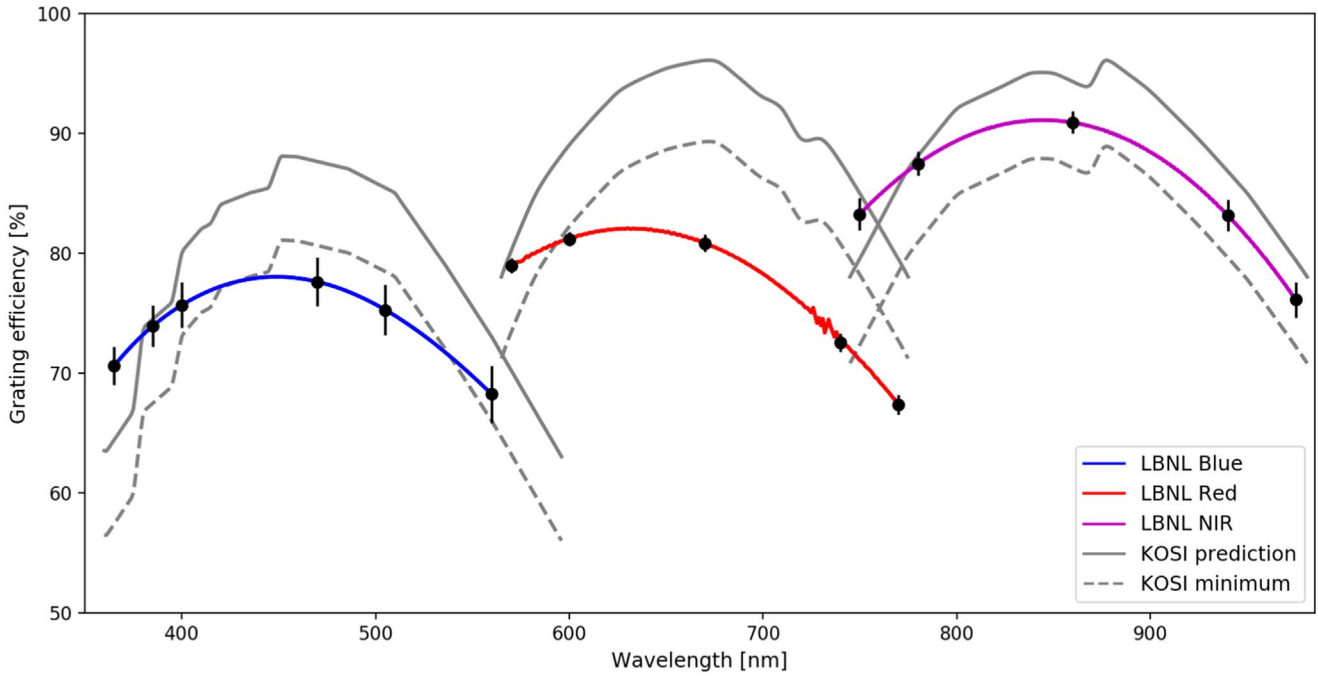


Figure 9. For each bandpass, the measured average area-weighted grating efficiencies and their uncertainties are plotted as symbols. The corresponding average spline interpolations are shown as colored curves. Two KOSI prediction curves are shown: theoretical predictions in solid gray and the minimal performances in dashed gray (J. Arns 2018, private communication). The small error bars highlight the consistency of the grating performances.

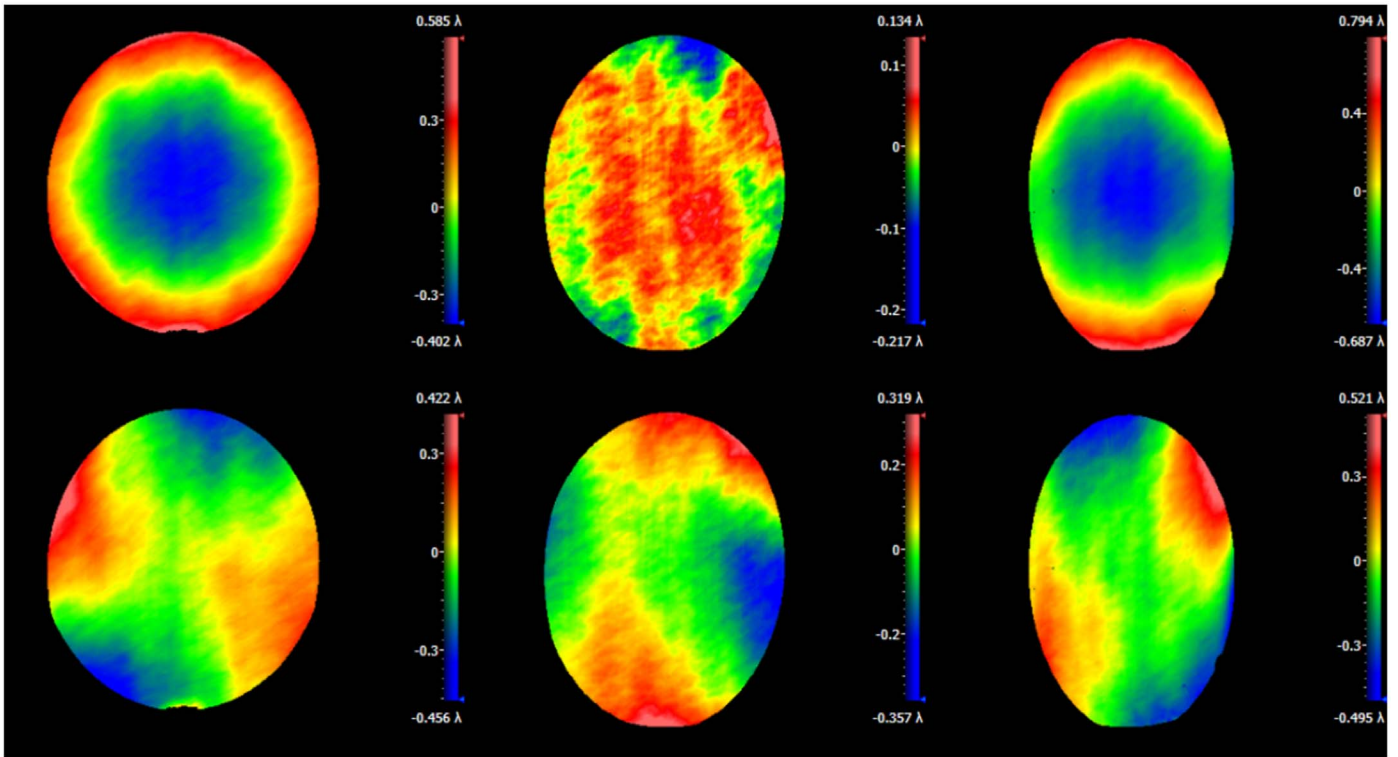


Figure 10. Measured wavefronts for the blue #64475 (left), red #64935 (center), and NIR #65754 (right) gratings. The top row shows the power wavefront and the bottom row shows the irregularity wavefront. The maps were produced with the Zygo Mx-Pro software. The color gradients used in the maps have not been normalized to the same wavelength scale.

discharge lamp, and revealed the wavelength uncertainty to be $\sigma_\lambda = \pm 0.7$ nm. Combining the uncertainty in beam-to-grating alignment $\sigma_\phi = \pm 0^\circ 07$, the grating rotation uncertainty $\sigma_\theta = \pm 0^\circ 01$, the uncertainty in the centering of the photodiode to the beam $\sigma_\beta = \pm 0^\circ 01$, and the wavelength uncertainty, we

find the total uncertainty in the measured α_0 is $\sigma_\alpha = \pm 0^\circ 07$. This is smaller than the rms spread of measured α_0 -angles, which is $\pm 0^\circ 4$ at most, indicating measurement errors of α_0 are minimal. Thus, the observed variations in α_0 between the gratings are an inherent property of them, most likely caused by

Table 6
P-V Wavefront Errors for Blue Gratings at 632.8 nm

Grating SN	Power P-V (wave)	Rms (wave)	Irregularity P-V (wave)	Rms (wave)
64467	0.244	0.058	0.526	0.091
64468	0.280	0.078	0.561	0.129
64469	0.301	0.087	0.490	0.097
64470	0.256	0.069	0.432	0.112
64471	0.264	0.072	0.441	0.079
64472	0.248	0.078	0.346	0.066
64473	0.286	0.146	0.310	0.117
64474	0.308	0.136	0.298	0.080
64475	0.283	0.116	0.274	0.073
64476	0.259	0.129	0.301	0.102
64477	0.123	0.045	0.275	0.114
64478	0.289	0.133	0.323	0.112
Average	0.262	0.096	0.382	0.098

Table 7
P-V Wavefront Errors for Red Gratings at 632.8 nm

Grating SN	Power P-V (wave)	Rms (wave)	Irregularity P-V (wave)	Rms (wave)
64935	0.155	0.021	0.226	0.064
64936	0.184	0.156	0.201	0.047
64937	0.092	0.025	0.246	0.089
64938	0.154	0.123	0.210	0.038
64939	0.308	0.006	0.226	0.046
64940	0.137	0.079	0.359	0.148
64941	0.124	0.067	0.291	0.100
64942	0.180	0.024	0.248	0.064
64443	0.189	0.125	0.239	0.079
64944	0.096	0.044	0.329	0.112
64945	0.118	0.069	0.332	0.126
64946	0.112	0.060	0.272	0.088
Average	0.154	0.067	0.265	0.083

Table 8
P-V Wavefront Errors for NIR Gratings at 632.8 nm

Grating SN	Power P-V (wave)	Rms (wave)	Irregularity P-V (wave)	Rms (wave)
65744	0.204	0.158	0.508	0.209
65745	0.172	0.130	0.306	0.090
65746	0.146	0.079	0.328	0.112
65747	0.233	0.055	0.306	0.076
65748	0.191	0.142	0.286	0.073
65749	0.322	0.041	0.409	0.076
65750	0.241	0.194	0.255	0.103
65751	0.174	0.091	0.293	0.091
65752	0.281	0.233	0.259	0.113
65753	0.156	0.105	0.249	0.081
65754	0.316	0.254	0.385	0.118
65755	0.236	0.174	0.430	0.172
Average	0.223	0.138	0.334	0.110

the quality and uniformity of the gelatin used to store the grating fringes.

Although VPH gratings are known to be mostly insensitive to polarization effects (Arns et al. 1999; Barden et al. 2000; Baldry et al. 2004), it is likely that there is some unaccounted-for shift in the rocking curve due to polarization effects,

especially since polarization of the source was not controlled or characterized. Fortunately, post-measurement analysis has shown that the knowledge of the properties of the sources used was sufficient to estimate possible uncertainties due to polarization. LEDs by nature do not produce polarized light, so polarization effects for the blue measurements are not applicable. On the other hand, the Newport monochromator used for the red and NIR gratings has several reflective surfaces, which would mean it may output partially polarized light. According to Newport, a similar model monochromator, Newport CS260, supposedly does not produce polarization (L. Pryde 2018, private communication). However, assuming the monochromator outputs 10% polarized light, we would only expect about 5% polarized light incident on the gratings; the 400 μm fiber feeding the monochromator light to the grating face was measured to preserve roughly 50% of incident polarization. Despite this, since the measured α_0 were consistent and were close to the design specifications, it was determined that polarization effects were minimal.

An advantage of the co-dependence between α_0 and $\eta(\lambda)$ of the VPH gratings is the ability to tune the efficiency profile with α , where the blaze profile can be shifted or tilted by simply changing the incident α angle (Barden et al. 2000). From Figure 5, we see that adjusting the α -angle would “rock” the ends of the efficiency curves about the blaze wavelength (hence “rocking curve”), boosting specific wavelength bands. This may be desirable depending on the science objectives. For example, one may choose a smaller α -angle for the blue gratings to boost the performance in the 350–400 nm UV band. Likewise, smaller α -angles for some NIR gratings may be desired to boost efficiency in the 750–800 nm band. On the other hand, larger α -angles for the red gratings would appear to boost the performance in the 700–750 nm. It is also possible to tune the rocking curves into a more symmetric shape about the blaze wavelength. This tuning feature would certainly be advantageous for the blue gratings, especially since these were measured at the non-optimal α_0 ; however, this would mean neglecting certain DESI spectrograph design constraints (Edelstein et al. 2018). Despite the apparent advantages of α -tuning, it is important to note that deviating from the optimal α_0 would result in a lower overall wavelength-averaged efficiency. Thus, the α -angle tuning feature should be examined with caution.

6.2. Rocking Curve Stability

The low statistical errors and measurement stability of the VPH efficiency, evident in the similar rocking curve shapes, indicate high consistency in the blaze optimization. A careful accounting of the $\bar{\eta}_\lambda$ indicates that the apparent asymmetry in the all measured rocking curves is a real feature of the gratings. We also note the efficiency profiles to be much broader and smoother, compared to the vendor predictions, which is preferable for a broadband redshift-survey like DESI.

In fact, despite the efficiency losses in the red gratings, both these and the NIR gratings showed remarkable consistency in their efficiency performances with an rms spread within 2.5% and 4.2% respectively. The blue gratings showed a larger variation in efficiency performance with a rms of 6.9%, shown in Figure 8. The spread in the blue performance may be indicative of the difficulties involved in producing thin-film VPH gratings optimized in the blue. In fact, there is an apparent correlation of the blue grating production order (serial

numbers) and $\bar{\eta}_\lambda$ (Table 3), where the $\bar{\eta}_\lambda$ appears to improve with increasing serial number, which may be suggestive of the fine-tuning involved in the UV–blue band VPH grating production. According to the vendor, an internal program to optimize the blue performance was conducted prior to full production of the DESI gratings; the detailed procedures were not disclosed (J. Arns 2018, private communication). On the other hand, the production orders of the red and NIR gratings do not appear to correlate with efficiency. There is no apparent correlation between optimal α_0 and the shape of the rocking curves, nor any correlation with $\bar{\eta}_\lambda$, indicating high reliability and consistency in VPH grating performance.

6.3. Off-axis Efficiency

Off-axis efficiency measurements at the optimal α_0 angle were also measured at $\pm 7^\circ 5$ from the grating axis through the grating center to simulate the input at the maximum FOV angle, as illustrated in Figure 2. A small scatter of $\pm 2\%$ in diffraction efficiency was observed for the off-axis input angles. This is comparable to the uncertainty of the detector measurement, so the dependence on incident FOV angle is insignificant. Since there were no DESI requirements on off-axis efficiency, no vendor measurements were made for comparison. The low loss in measured efficiency at the most extreme FOV angles was deemed sufficient for DESI, so no further effort was made to explore the off-axis dependence.

6.4. WFE

As described in Section 4, the test configuration measures the WFEs at different incidence angles than they were designed for. The incidence angles were arbitrarily chosen to avoid clipping, and the gratings were illuminated at 632.8 nm, which is out-of-band in the blue and NIR bandpasses. These measurement parameters would suggest poor signal-to-noise or even additional wavefront aberrations. Despite these concerns, Zygo measurements have shown sufficient signal-to-noise ratio for all gratings. In fact, the α -angle tuning feature had worked to our advantage with blue gratings, as the larger α -angles boost the red-band efficiency for high signal-to-noise. Also, although the rocking curves suggest low 632.8 nm efficiency for the NIR gratings at $\alpha \approx -50^\circ$, there was sufficient signal-to-noise ratio for wavefront measurements.

Also, since post-polishing of the substrates was not required by DESI, it is possible that roughness in the substrates may contribute to the measured WFEs. However, both the measured P-V power and irregularity errors, listed in Tables 6–8, show remarkable consistency with an average spread of roughly 0.05 waves for each grating type, which is highly preferable for the DESI experiment. We see that the measured P-V errors safely meet the DESI specifications.

7. Conclusion

This paper describes a thorough performance test methodology by presenting evaluation results for a production run of VPH gratings made for the DESI experiment. A custom measurement rig was built to measure the grating performance, summarized as follows.

1. The incidence angles for the red and NIR gratings met design specifications, while the blue gratings exceeded

the allowed installation window of $\pm 1^\circ 0$. All measured α_0 s were consistent to within $\pm 0^\circ 5$.

2. Minimal ($< 2\%$) off-axis incidence angle dependence in efficiency was observed, despite the lack of specification provided to the vendor.
3. The wavelength-averaged efficiency of the blue and NIR gratings comfortably met their respective throughput requirements. On the other hand, the red gratings exhibited performance losses focused in the $\lambda > 700$ nm region, with the average efficiency measured to be 2.4% below the DESI requirements. Efficiency at the central wavelengths for all gratings was found to meet the design requirements. The overall efficiency–wavelength relations are recorded in their respective rocking curves.
4. With the exception of one NIR grating, the P-V power and irregularity WFE were determined to meet specifications with high consistency.

Despite some spread in performance levels, measurements showed a high level of consistency in VPH grating efficiency performance, rocking curve shapes, and incidence angles for each bandpass set, which is important for the DESI experiment. The consistency in measured performances from the statistically significant sample of specific grating designs affords a very useful insight into the maturity of VPH fabrication techniques, the expected performance uniformity within a larger production batch, or even the likelihood of meeting some specification goals for a single grating unit with comparable characteristics. This characteristic of VPH gratings is extremely important, especially as the reliance on them as dispersers becomes more common in the era of extremely large telescopes and powerful transient factories, instruments that use highly replicated unit spectrographs. Based on these measurements, the VPH gratings have been approved for the DESI spectrograph integration, and will serve as a valuable step in preparing DESI to better understand the nature of the universe.

This research is supported by the Director, Office of Science, Office of High Energy Physics of the U.S. Department of Energy under Contract No. DEAC0205CH1123, and by the National Energy Research Scientific Computing Center, a DOE Office of Science User Facility under the same contract; additional support for DESI is provided by the U.S. National Science Foundation, Division of Astronomical Sciences under Contract No. AST-0950945 to the National Optical Astronomy Observatory; the Science and Technologies Facilities Council of the United Kingdom; the Gordon and Betty Moore Foundation; the Heising-Simons Foundation; the National Council of Science and Technology of Mexico, and by the DESI Member Institutions. The authors are honored to be permitted to conduct astronomical research on Iolkam Duag (Kitt Peak), a mountain with particular significance to the Tohono O’odham Nation.

We would like to express the utmost gratitude to all involved in making this project possible. We would like to especially thank William Van Shourt and Jeremy McCauley for the engineering developments, Dmitriy Voronov for assisting with wavefront measurements, and Steve Gibson for the helpful suggestions. We are especially grateful to Charles Baltay, Michael Lampton, and Timothy N. Miller for the valuable input and discussions in improving this paper. We acknowledge and thank James A. Arns of Kaiser Optical Systems, Inc.,

an Endress+Hauser Company, for the development of the VPH gratings. Finally, we thank the DESI Collaboration and the LBNL staff.

Appendix A Efficiency Measurements

The optimal incidence angle α_0 and average area-weighted efficiencies with corresponding averages and rms variations for all 12 VPH gratings measured are shown in the following tables. The VPH gratings are listed in order of best-to-worst wavelength-averaged, area-weighted efficiency $\bar{\eta}_\lambda$. See Table 2 for statistics on the top 10 blue, red, and NIR gratings. The VPH gratings can be identified by their serial number (SN). Italicized text indicates interpolated values and average efficiencies calculated using these.

Appendix B P-V Wavefront Error Measurements

The measured P-V wavefront errors for all 12 VPH gratings measured are shown in the following tables. The VPH gratings are listed in order identified by their serial number (SN).

ORCID iDs

Yuzo Ishikawa  <https://orcid.org/0000-0001-7572-5231>
David Brooks  <https://orcid.org/0000-0002-8458-5047>
Gregory Tarle  <https://orcid.org/0000-0003-1704-0781>

References

- Abbott, T. M. C., Abdalla, F. B., Allam, S., et al. 2018, arXiv:1801.03181
- Arns, J. A., Colburn, W. S., & Barden, S. C. 1999, *Proc. SPIE*, 3779, 3779
- Baldry, I. K., BlandHawthorn, J., & Robertson, J. G. 2004, *PASP*, 116, 403
- Barden, S. C., Arns, J. A., & Colburn, W. S. 1998, *Proc. SPIE*, 3355, 3355
- Barden, S. C., Arns, J. A., Colburn, W. S., & Williams, J. B. 2000, *PASP*, 112, 809
- Barden, S. C., Arns, J. A., Colburn, W. S., & Williams, J. B. 2002, *Proc. SPIE*, 4485, 429
- Bass, M. 1994, *Handbook of Optics*, Vol. 2 (New York: McGraw-Hill Professional)
- Blanche, P.-A., Habraken, S., Lemaire, P., & Jamar, C. 2006, *ApOpt*, 45, 6910
- Burgh, E. B., Bershad, M. A., Westfall, K. B., & Nordsieck, K. H. 2007, *PASP*, 119, 1069
- DESI Collaboration, Aghamousa, A., Aguilar, J., et al. 2016a, arXiv:1611.00036
- DESI Collaboration, Aghamousa, A., Aguilar, J., et al. 2016b, arXiv:1611.00037
- Dey, A., Schlegel, D. J., Lang, D., et al. 2018, arXiv:1804.08657
- Edelstein, J., Jelinsky, P., Levi, M., Tarle, G., & Brooks, D. 2018, *Proc. SPIE*, 10702, 107027G
- Evans, C. 2008, in *Frontiers in Optics 2008/Laser Science XXIV/Plasmonics and Metamaterials/Optical Fabrication and Testing* (Washington, DC: Optical Society of America), OWA4
- Evans, C. J. 2009, *OptEn*, 48, 043605
- LSST Science Collaboration, Abell, P. A., Allison, J., et al. 2009, arXiv:0912.0201
- Martini, P., Bailey, S., Besuner, R. W., et al. 2018, *Proc. SPIE*, 10702, 107021F
- Perlmutter, S., Aldering, G., Goldhaber, G., et al. 1999, *ApJ*, 517, 565
- Poppett, C., Sharples, R., Edelstein, J., et al. 2016, *Proc. SPIE*, 9908, 99089A
- Riess, A. G., Filippenko, A. V., Challis, P., et al. 1998, *AJ*, 116, 1009
- Zecchino, M. 2014, *Setting the Wedge Factor*, Tech. Rep., 4D Technology Corporation, <https://www.4dtechnology.com/library/Setting-the-Wedge-Factor-Tech-Note.pdf>